2012

# Cool and warm dust emission from M33 (HerM33es)

E. M. Xilouris
F. S. Tabatabaei
M. Boquien
C. Kramer
C. Buchbender, et al.

# Cool and warm dust emission from M33 (HerM33es)[⋆]

E.M. Xilouris[1], F.S. Tabatabaei[2], M. Boquien[3], C. Kramer[4], C. Buchbender[4], F. Bertoldi[5], S. Anderl[5],
J. Braine[6], S. Verley[7], M. Relaño[7], G. Quintana-Lacaci[4], S. Akras[8], R. Beck[9], D. Calzetti[10], F. Combes[11],
M. Gonzalez[4], P. Gratier[12], C. Henkel[9,13], F. Israel[14], B. Koribalski[15], S. Lord[16], B. Mookerjea[17],
E. Rosolowsky[18], G. Stacey[19], R.P.J. Tilanus[20,21], F. van der Tak[22], and P. van der Werf[14,23]

(Affiliations can be found after the references)

**ABSTRACT**

We study the far-infrared emission from the nearby spiral galaxy M33 in order to investigate the dust physical properties such as the temperature and the luminosity density across the galaxy. Taking advantage of the unique wavelength coverage (100, 160, 250, 350 and 500 $\mu$m) of the Herschel Space Observatory and complementing our dataset with Spitzer-IRAC 5.8 and 8 $\mu$m and Spitzer-MIPS 24 and 70 $\mu$m data, we construct temperature and luminosity density maps by fitting two modified blackbodies of a fixed emissivity index of 1.5. We find that the "cool" dust grains are heated at temperatures between 11 and 28 K with the lowest temperatures found in the outskirts of the galaxy and the highest ones in the center and in the bright HII regions. The infrared/submillimeter total luminosity (5 - 1000 $\mu$m) is estimated to be $1.9 \times 10^9 \, {}^{+4.0\times10^8}_{-4.4\times10^8}$ L$_\odot$. 59% of the total luminosity of the galaxy is produced by the "cool" dust grains ($\sim$ 15 K) while the rest 41% is produced by "warm" dust grains ($\sim$ 55 K). The ratio of the cool-to-warm dust luminosity is close to unity (within the computed uncertainties), throughout the galaxy, with the luminosity of the cool dust being slightly enhanced in the center of the galaxy. Decomposing the emission of the dust into two components (one emitted by the diffuse disk of the galaxy and one emitted by the spiral arms) we find that the fraction of the emission in the disk in the mid-infrared (24 $\mu$m) is 21%, while it gradually rises up to 57% in the submillimeter (500 $\mu$m). We find that the bulk of the luminosity comes from the spiral arm network that produces 70% of the total luminosity of the galaxy with the rest coming from the diffuse dust disk. The "cool" dust inside the disk is heated at a narrow range of temperatures between 18 and 15 K (going from the center to the outer parts of the galaxy).

**Key words.** galaxies: individual: M33 - galaxies: Local Group - galaxies: spiral

## 1. Introduction

Studies of the dust content and of the properties of the interstellar medium (ISM) within nearby galaxies have been a major topic of research since the launch of the *Infrared Astronomical Satellite (IRAS)*. The IRAS measurements at 60 $\mu$m and 100 $\mu$m, being sensitive in detecting the emission from the warm dust ($\sim$ 45 K) peaking at these wavelengths, provided a unique database for studying this fraction of the total ISM (e.g. Young et al., 1996, Devereux & Young 1990). With the advent of the *Infrared Space Observatory (ISO)* and the *Spitzer Space Telescope*, measuring at wavelengths greater than 100 $\mu$m, as well as the submillimeter (submm) observations by the *James Clerk Maxwell Telescope (JCMT)*, it became evident that the bulk of the dust grains reside in a cooler (below 20 K) component making the most significant contribution to the total far-infrared (FIR) and submm emission of a galaxy. Although the existence of the warm and cool components is now well established, spatial information on their distribution of their emission within galaxies is still an issue. Galaxies showing prominent spiral structure in optical

wavenegths show strong dusty spiral arms as well as dust material diffusely distributed throughout the galaxy revealing itself in the inter-arm regions (e.g., Haas et al., 1998; Gordon et al., 2006; Hippelein et al. 2003). A simplistic, nevertheless elegant, way to distinguish between the dust diffusely distributed throughout the galaxy and the dust situated inside the spiral arms is to assume that the spiral arm network is superimposed on an axisymetric dusty disk (e.g. Misiriotis et al. 2000; Meijerink et al. 2005). *Herschel Space Observatory* (Pilbratt et al. 2010) with its unique wavelength coverage, resolving power, and sensitivity is an excellent source of data for such studies.

The galaxies in the Local Group, because of their proximity, are ideal systems for carrying out high spatial resolution studies of the interstellar medium (ISM). M33, an Sc spiral galaxy at a distance of 840 kpc (Freedman et al. 1991), is an ideal candidate for the present analysis. Already mapped by ISO at 60, 100 and 170 $\mu$m at a moderate resolution, M33 reveals a spiral structure with a large number of distinct sources, as well as a diffuse extended component (Hippelein et al., 2003). In the same study, spectral energy distributions (SEDs) constructed for the central part of the galaxy as well as the interarm regions and prominent HII regions, reveal typical temperatures of $T_w \sim 46$ K for the warm dust and $T_c \sim 17$ K for the cool dust component. Performing a multi-scale study of the infrared emission of M33 using Spitzer-MIPS data and a wavelet analysis tech-
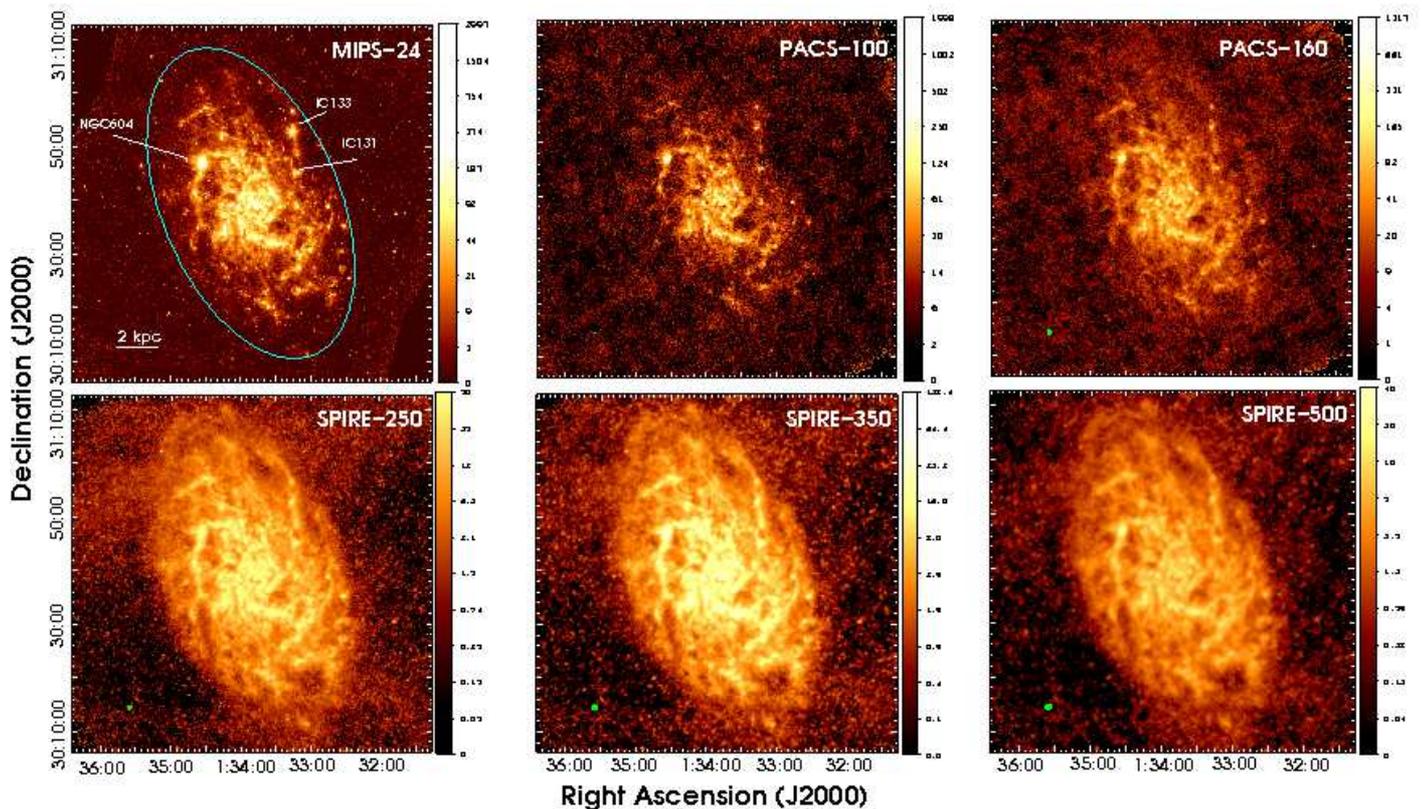
**Fig. 1.** Spitzer MIPS-24 $\mu$m (upper left panel), Herschel PACS-100 and 160 $\mu$m (upper middle and right panels, respectively) and SPIRE-250, 350 and 500 $\mu$m (lower left, middle and right panels, respectively). All maps are at their original resolution with the FWHM of the beams ($6''$, $6.7'' \times 6.9''$, $10.7'' \times 11.1''$, $18.3'' \times 17.0''$, $24.7'' \times 23.2''$, $37.0'' \times 33.4''$ for 24, 100, 160, 250, 350, 500 $\mu$m respectively) indicated as green circles at the bottom-left part in each panel. In the MIPS-24 $\mu$m map, three of the brightest HII regions labeled for reference. The outer ellipse shows the B-band $D_{25}$ (semi-major axis length = 7.5 kpc; Paturel et al. 2003) extent of the galaxy. The brightness scale is given in units of MJy sr$^{-1}$.

nique, Tabatabaei et al. (2007a) concluded that most of the 24 and 70 $\mu$m emission emerge from bright HII regions and star-forming complexes, while the 160 $\mu$m emission traces both compact and diffuse emission throughout the galaxy. Using the intensity maps at 70 and 160 $\mu$m Tabatabaei et al. (2007b) constructed temperature maps showing variations of the temperature between 19 and 28 K while similar conclusions were reached by Verley at al. (2008) by constructing the dust temperature variations as a function of radius from the center.

The recently launched Herschel Space Observatory offers the possibility to study M33 at FIR and submm wavelengths in more detail than possible before. The PACS (Poglitsch et al. 2010) and SPIRE (Griffin et al. 2010) instruments combined allow to produce images over the wavelength range between 70 and 500 $\mu$m with unprecedented sensitivity and superior resolution. In this paper we use PACS (100 $\mu$m and 160 $\mu$m) and SPIRE (250 $\mu$m, 350 $\mu$m, 500 $\mu$m) imaging, taken as part of the Herschel M33 extended survey (HerM33es; Kramer et al. 2010), an open time key project, along with a two component modified blackbodies model in order to better understand the continuum emission of M33. With this approach we hope to shed some light on the temperature and luminosity distributions of M33, being aware of the simplistic nature of the model that is used. A more realistic analysis (within the framework of the HerM33es is presented elsewhere (Rosolowsky

et al., in prep). In Section 2 we present the observations and the data reduction techniques that we use, Section 3 gives a brief description of the morphology of the galaxy at the Herschel wavelengths, Section 4 describes modeling of the data, while the results of our study are presented in Section 5 and discussed in Section 6. We, finally, present our conclusions in Section 7.

## 2. Observations and data reduction

M33 was observed on 7 and 8 January 2010 with PACS and SPIRE covering a field of $70' \times 70'$. Observations were made using the PACS and SPIRE parallel mode with a scanning speed of $20''/s$ providing simultaneous observations at 100 $\mu$m and 160 $\mu$m as well as at 250 $\mu$m, 350 $\mu$m, and 500 $\mu$m. The PACS maps presented in this paper were reduced using the scanamorphos algorithm (Roussel 2012) discussed in detail in Boquien et al., (2011) and in Rosolowsky et al., (in prep.). SPIRE maps were reduced using HIPE 7.0 (Ott 2010) and the SPIRE calibration tree v. 7.0. SPIRE characteristics (point spread function, beam area, bandpass transmission curves, correction factors for extended emission) were taken from the SPIRE Observers' Manual (v2.4, 2011). A baseline algorithm (Bendo et al. 2010) was applied to every scan of the maps in order to correct for offsets between the detector timelines and remove residual baseline signals. Finally, the maps were cre-
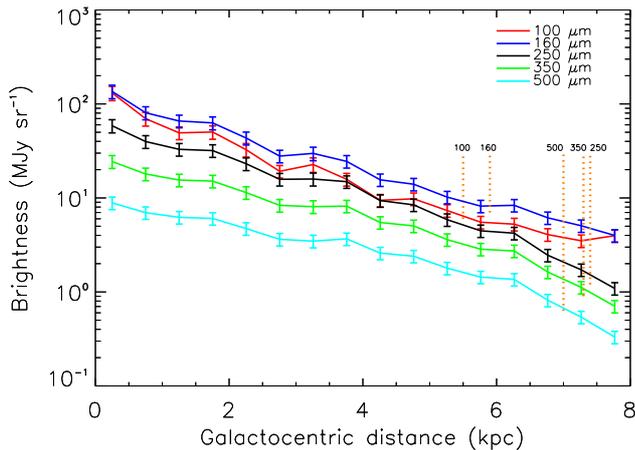
**Fig. 2.** Azimuthally averaged radial profiles, projected on the major axis of M33 for the 100, 160, 250, 350 and 500 $\mu$m emission (red, blue, black, green and cyan colors respectively). The vertical dotted lines (in orange colour) indicate the 3-$\sigma$ flux level threshold for each wavelength.

**Fig. 3.** Histogram of the $\chi^2_{red}$ values for the three models with $\beta = 1$, 1.3, 1.5, 1.7 and 2 (cyan, green, red, blue and black line respectively).

ated using a "naive" mapping projection. For the errors in the PACS and SPIRE photometry we adopted a conservative 15% calibration uncertainty for extended emission (Boquien et al., 2011; SPIRE Observers' Manual, v2.4, 2011).

In addition to the Herschel maps we also used the, publicly available mid-infrared (MIR) maps, at 5.8, and 8 $\mu$m obtained with the IRAC instrument, and the 24 and 70 $\mu$m obtained with the MIPS instrument on-board the Spitzer Space Observatory. To account for the stellar pollution in the 5.8 and 8 $\mu$m fluxes we used the IRAC-3.6 $\mu$m data as a reference point assuming that fluxes at this waveband traces stellar emission only. This, however, is a crude approximation since dust contamination, especially in the bright HII regions, may be present in 3.6 $\mu$m. We then corrected the 5.8 and 8 $\mu$m maps by assuming a stellar light contamination dictated by the 3.6 $\mu$m measurements scaled with a Rayleigh-Jeans law.

The maps that were used in our analysis were all convolved to a common angular resolution (the resolution of the 500 $\mu$m SPIRE image; approximately 40″) by using the dedicated convolution kernels provided by Aniano et al. (2011)[1] and projected to the same grid (of a 10″pixel) and center position.

## 3. Morphology

Figure 1 shows the maps obtained at the five Herschel wavelengths (100, 160, 250, 350 and 500 $\mu$m) as well as the 24 $\mu$m map for comparison. In the 24 $\mu$m map we have also marked the B-band $D_{25}$ (7.5 kpc; Paturel et al. 2003) extent of the galaxy as well as the three of the brightest HII regions. All maps are at their original resolution with the brightness scale in MJy sr$^{-1}$.

We use the Herschel maps to spatially model the SED across the galaxy (see Sect. 4). All Herschel maps clearly show the spiral arm structure and a large number of distinct
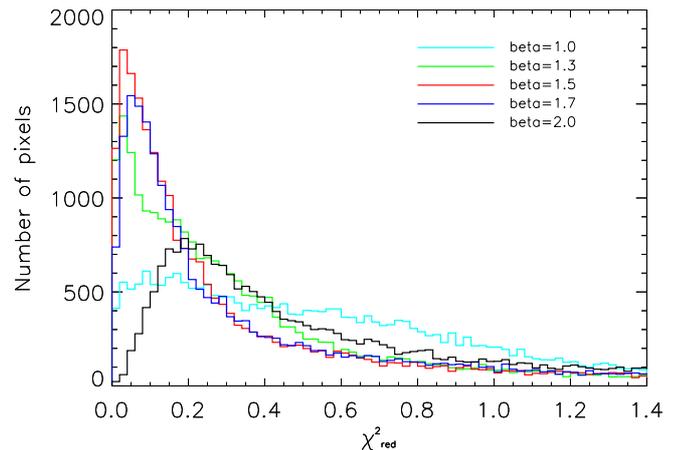
---

[1] http://www.astro.princeton.edu/~ganiano/Kernels.html

sources. In addition to the spiral structure, an extended underlying emission component can be recognized (especially evident in the three SPIRE maps). This is better illustrated by the azimuthally averaged radial profiles presented in Fig. 2. The averaging in these profiles is made within successive elliptical rings of 500 pc width and a minor-to-major axis ratio of 0.54 accounting for an inclination of 56 degrees (Regan & Vogel 1994). The profiles are plotted all the way out to 8 kpc with the orange vertical lines indicating the 3-$\sigma$ threshold in each band. To these profiles we have fitted exponential functions (minimizing the $\chi^2$) in order to derive the characteristic scalelength of the dust emission at each wavelength. We have done that for the range of radii with fluxes above the 3-$\sigma$ threshold. We find scalelengths of 1.84 ± 0.12 kpc, 2.08 ± 0.09 kpc, 2.14 ± 0.08 kpc, 2.50 ± 0.12 kpc and 3.04 ± 0.15 kpc for the 100 $\mu$m, 160 $\mu$m, 250 $\mu$m, 350 $\mu$m and 500 $\mu$m, respectively. The value for the scalelength that we derive for the 160 $\mu$m emission using the Herschel-PACS data is in excellent agreement with the value obtained using the Spitzer-MIPS data (1.99±0.02 kpc; Verley et al. 2009). The flatter dust distribution at longer wavelengths is indicative of a more extended distribution which is related to emission dominated by "cool" ($\sim$ 15 K) dust grains (see Sect. 6.1). Similar conclusions have been reached by others using ISO (e.g., Alton et al. 1998; Davies et al. 199) and Herschel (e.g., Bendo et al. 2012) observations.

The spiral arms in all Herschel bands can be traced all the way to the center of the galaxy (to a 30 pc scale; which is roughly the PACS 100 $\mu$m resolution). Two main spiral arms, one to the north-east and one to the southwest, are the brightest large-scale features of the galaxy. The main spiral structure is also present at optical, near-infrared (NIR), and radio wavelengths (Block et al. 2007; Tabatabaei et al. 2007b). Apart from these two open spiral arms our observations show numerous, apparently independent, long-arm spirals in the outer region of the galaxy, with a smaller pitch angle. This appears like a flocculent spiral structure, while in the NIR two arcs or wound spiral arms delineate another coherent pattern. M33 is not the only galaxy showing a flocculent spiral structure in young

tracers, like gas and young stars, superposed to a more grand-design spiral structure (e.g. Block et al. 1996). These branched multiple spirals could be random and independent wave packets triggered by local gravitational instabilities in the gas and stars (Binney & Tremaine 1987) or they could result entirely from propagating star formation and differential rotation (Gerola & Seiden 1978). In this case, gaseous instabilities trigger a first star formation leading to supernova explosions and shell-like compressions in the ISM. This triggers more star formation leading to a chain reaction in which aggregates of stars are created (see, e.g., Verley et al. 2010). The differential rotation of the galaxy, then, stretches these aggregates into spiral arcs. A characteristic picture of such violent processes is also evident in M33 with a huge ($> 1$ kpc) shell-like feature which appears to break the south-west spiral arm (evident in all Herschel maps of Fig. 1). A detailed analysis of the morphology of the gas and dust content of M33 is presented in Combes et al. (2012) using power-spectrum analysis techniques.

This picture is in excellent agreement with other tracers of the ISM such as the atomic and the molecular hydrogen (Braine et al. 2010; Gratier et al. 2010; Gratier et al. 2011). Many localized infrared sources are well detected in the Herschel bands. These sources are mainly HII regions situated in the spiral arms showing enhanced star-formation activity. A detailed analysis of the properties of these sources is presented in Verley et al. (2010) as well as in Boquien et al. (2010).

## 4. The model

The unprecedented spatial resolution in the FIR and submm wavelengths obtained with Herschel allows us to study the dust grain properties at a very small scale throughout the galaxy. For this purpose the dust SED was modeled assuming optically thin emission described by two modified blackbodies, one accounting for the "cool" dust emission, originating from the large grains being heated by the local and the diffuse galactic radiation field, and one accounting for the "warm" dust emission, originating from the grains being heated in dense and warm environments where star formation is taking place. According to this model the emission at a given frequency ($\nu$) is described by:

$$S_\nu = \frac{1}{\lambda^\beta}[N_c B(\nu, T_c) + N_w B(\nu, T_w)] \qquad (1)$$

where $B(\nu, T)$ is the Planck function, and $T_c$, $T_w$ are the dust temperatures for the "cool" and the "warm" dust component respectively, $\beta$ is the emissivity index while $N_c$ and $N_w$ are normalization constants related to the dust column density in each of the "cool" and the "warm" components respectively. To find the best SED for each pixel on the map, our code minimizes the $\chi^2$ function ($\chi^2 = \sum((S_{\nu,obs} - S_\nu)/\Delta S_{\nu,obs})^2$) using the Levenberg-Marquardt algorithm (Bevington & Robinson 1992). The model was applied to the 24, 70, 100, 160, 250, 350 and 500 $\mu$m maps regridded to a common resolution and pixel size (see Sect. 2) and for all pixels with intensities larger than 3 times the rms noise level. The rms noise level for the (FWHM=40$''$ and pixel size=10$''$) maps that we used are 0.012, 0.31, 3.2, 3.4, 0.64, 0.50 and 0.32 mJy pix$^{-1}$ for the 24, 70, 100, 160, 250, 350 and 500 $\mu$m respectively. These
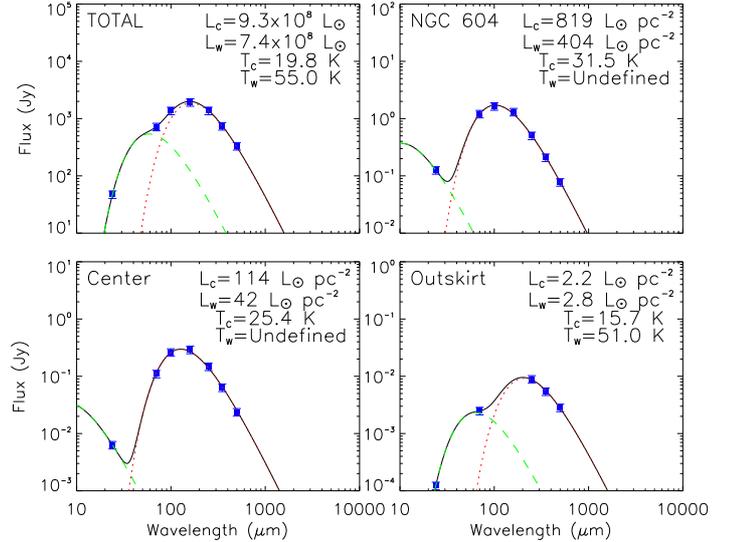


**Fig. 4.** SEDs, for the total galaxy (upper left panel) and for a typical HII region (upper right - center of NGC 604), as well as for the center of the galaxy (lower left panel), and for the "diffuse", outer part of the galaxy (lower right panel). The emission was modeled with two modified blackbodies of $\beta$=1.5 and fitted to the MIPS 24 and 70 $\mu$m, PACS 100 and 160 $\mu$m, and SPIRE 250, 350 and 500 $\mu$m observations. For the bright parts of the galaxy (around the center and in bright HII regions) it is evident that the specific model is not able to accurately describe the data giving unphysically high temperatures for the "warm" dust component. In the text we describe two different and more reliable methods to derive the properties of the "warm" dust component (see Sect. 4.1 for more details).

values were obtained by performing the statistics in regions well outside the galaxy. In order to expand our modeling to fainter parts of the galaxy (further than the distances allowed by the 3-$\sigma$ criterium to all available observations) we constrained the model by using the 24, 70, 250, 350 and 500 $\mu$m fluxes only (i.e., dropping the low signal-to-noise 100 and 160 $\mu$m measurements in the outer parts of the galaxy). These signal-to-noise considerations allow for the 47% of the galaxy's area to be modeled by using the full dataset (7 wavelengths) while for the rest 53% (mostly the outermost parts of the galaxy) the model is constrained by measurements in 5 wavelengths. We note here that, at this point of the analysis, we do not make use of the 5.8 and 8 $\mu$m fluxes to constrain the model. These observations will be used later in order to calculate the "warm" dust component of the SED (see Sect. 4.1). To adjust for the filter bandpasses the SED was convolved with the filter transmission before entering the $\chi^2$ minimization process. Based on the $\chi^2$ minimization, best fitted temperatures and luminosity densities were obtained.

In order to compute the uncertainty in the derived parameters we fitted the model to fluxes obtained within the uncertainty range of the observed fluxes. This was done by generating random deviates with a normal distribution (centered in the observed flux; Press et al. 1986). For this purpose, 2000 such mock datasets were created which, after fitted by the SED model, resulted into a set of 2000 values for each fitted parameter. From this distribution the
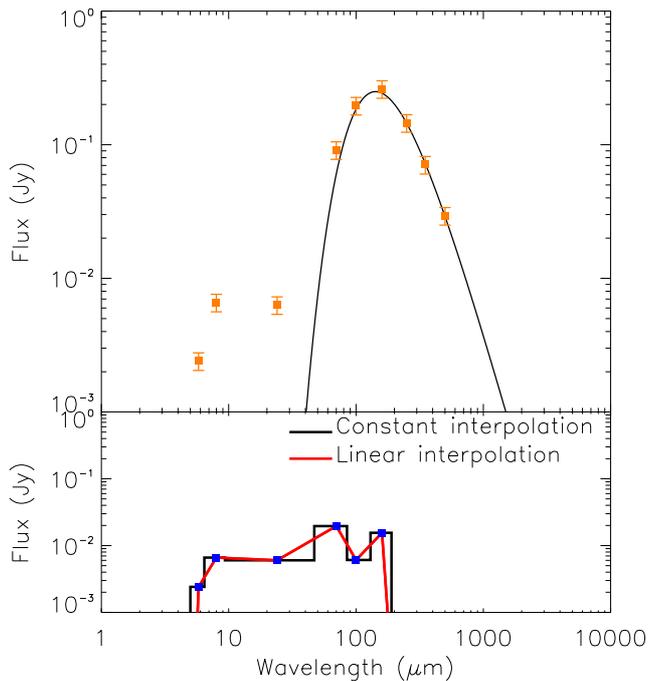
**Fig. 5.** Two of the techniques adopted to estimate the "warm" dust luminosity. After computing the "cool" dust component (top panel) the residual MIR, FIR and submm fluxes were calculated (blue points in the bottom panel). These residual fluxes were then integrated using (a) constant values within specified wavelength ranges according to the filter passbands (black lines) and (b) a linear interpolation between successive measurements (red lines). The pixel used for this demonstration is centered at 01:34:14.64, +30:34:31.57.

90% confidence intervals were determined and lower and upper limits were assigned on the best fitted value of each parameter.

The model dependence on the dust emissivity index $\beta$ was first explored by examining the change in $\chi^2$ for different $\beta$ values. Fig. 3 shows the histogram of the reduced $\chi^2_{red}$ values (the $\chi^2$ divided by the number of observed parameters minus the number of the fitted parameters minus one) for $\beta = 1$, 1.3, 1.5, 1.7 and 2. From this plot it is evident that the values close to $\beta = 1.5$ account for more points with the minimum $\chi^2_{red}$ indicating a better match between observations and model within the error variance of the data. The peak values of the histograms correspond to $\chi^2_{red}$ of $\sim$ 0.17, 0.02, 0.02, 0.06 and 0.19 for $\beta$=1, 1.3, 1.5, 1.7 and 2 respectively with the $\beta = 1.5$ distribution being the narrowest one. This value of $\beta$ is in good agreement with the best fitting value found by Kramer et al. (2010) in azimuthally averaged fluxes in elliptical rings. It is also in good agreement with statistical studies of galaxies (e.g., Dunne & Eales (2001), Yang & Phillips (2007), Benford & Staguhn (2008)). A comprehensive analysis on the dust emission dependence with $\beta$ (within the framework of the HerM33es Key Project) is presented elsewhere (Tabatabaei et al. 2011).
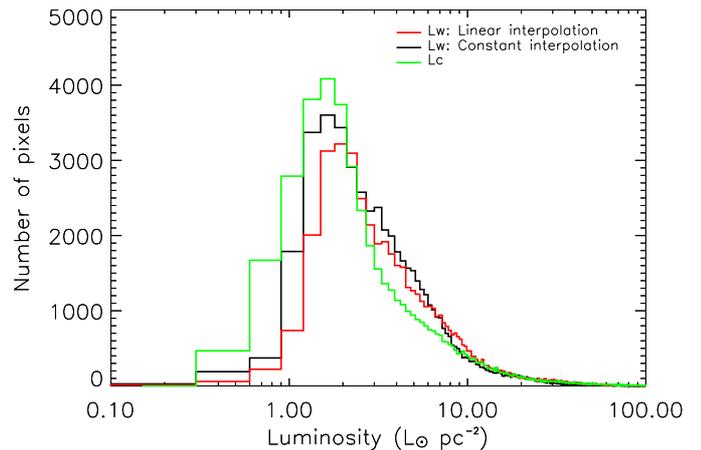


**Fig. 6.** The histogram of the luminosity densities of M33 which are produced by the "cool" dust component (green) and the "warm" dust component (red and black). The "cool" part of the luminosity was derived by fitting the SED with a two modified blackbodies ($\beta = 1.5$) model. The "warm" part of the luminosity is computed using the residual fluxes of the SED, derived after subtracting the "cool" dust component (see Fig. 5), and adopting two approximations for integrating the residual SED by a constant interpolation (black line) and a linear interpolation (red line) between the successive fluxes (see the text for more details).

### 4.1. The "warm" dust component of the SED.

The "warm" dust component is a highly unconstrained parameter of our model. This is because the simple model that we use is not capable of accurately describing the heating of the small dust grains emitting at short wavelengths. This is especially a very important caveat of the model when fitting bright parts of the galaxy like the central region and the cores of the bright HII regions. In these regions, the largest part of the SED is adequately well fitted by the "cool" component leaving only one flux measurement (at 24 $\mu$m) to constrain the "warm" part of the SED. It is, nevertheless, the unphysically large values of the "warm" dust temperatures and luminosities as well as the large uncertainties in these parameters that make this model inadequate to account for this part of the SED. Clearly, a more realistic model, taking into account dust emission at shorter, MIR, wavelengths is needed for a more complete determination of the dust properties of the galaxy (Rosolowski et al. in prep.).

Typical examples of single-pixel SEDs are shown in Fig. 4. The upper right panel presents an SED near the peak of the NGC 604 HII region (01:34:34.09, +30:46:51.25), the lower left panel shows an SED in the center of the galaxy (01:33:45.21, +30:38:41.69), while a faint, diffuse, part in the outskirts of the galaxy (01:32:42.54, +30:30:50.58) is presented in the lower right panel. The SED in the last position shows a typical case where only five flux measurements (PACS excluded; see Sect. 4) are used to constrain the model. From these SEDs the lack of data points shorter than 24 $\mu$m becomes evident in the brightest parts of the galaxy (NGC 604 and center of the galaxy) with the model failing in simulating the "warm" dust emission giving un-
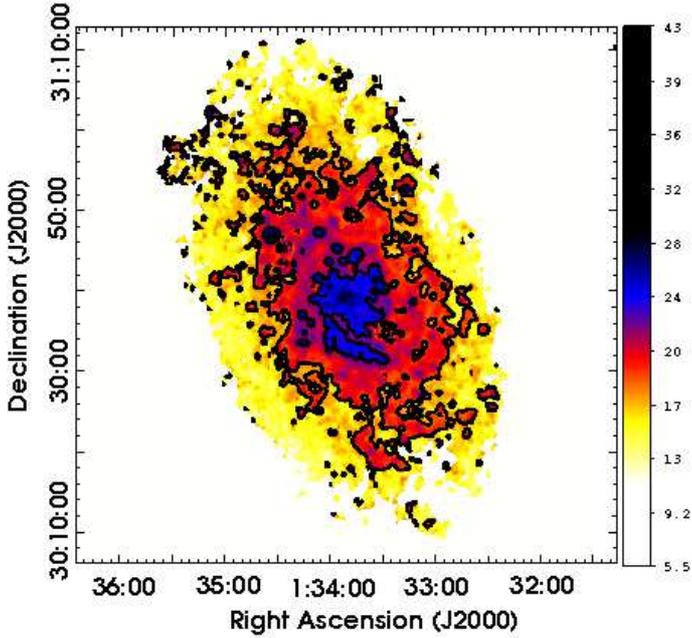
**Fig. 7.** The "cool" temperature ($T_c$) distribution across the galaxy. The two isothermal contours delineate regions with $T_c < 18$ K (yellow areas), $18$ K $< T_c < 23$ K (red/orange areas) and $T_c > 23$ K (blue areas).
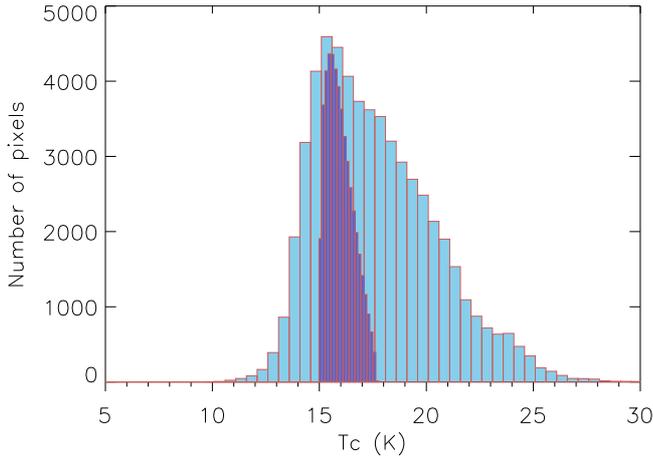


**Fig. 8.** The "cool" temperature ($T_c$) histogram distribution. The values derived for the whole galaxy are shown in the light blue histogram while the dark blue accounts only for the diffuse disk of the galaxy (see Sect. 6.2).

physically large values for the temperature of this component.

In order to get an estimate of the energy output of M33 which is linked to the star forming activities that are taking place inside the galaxy (the "warm" part of the SED) we compute the luminosity of the residual fluxes (after having subtracted the well defined "cool" component of the SED as computed above; see Fig. 5). We do so, in a pixel by pixel basis, by integrating the residual fluxes assuming a constant interpolation between successive wavelengths (see an example in Fig. 5). In particular, we assume the 5.8, 8, 24, 70, 100, 160, 250, 350 and 500 $\mu$m residual fluxes to be constant in the wavelength ranges of 5 - 6.44 $\mu$m,

6.44 - 9.34 $\mu$m, 9.34 - 47 $\mu$m, 47 - 85 $\mu$m, 85 - 130 $\mu$m, 130 - 190 $\mu$m, 190 - 300 $\mu$m, 300 - 400 $\mu$m and 400 - 1000 $\mu$m respectively (see the residual plot in Fig. 5). The wavelength ranges for the 5.8, 8, 250, 350 and 500 $\mu$m residual fluxes were dictated by the actual width of the IRAC and SPIRE passbands with the 500 $\mu$m range extended up to 1000 $\mu$m. For the MIPS and the PACS measurements we used the mid-point between successive wavelengths as the wavelength limit. With this method we compute a "warm" dust luminosity of $7.8 \times 10^8 {}^{+2.1 \times 10^8}_{-3.5 \times 10^8}$ L$_\odot$ of the entire galaxy. We note here that the well constrained "cool" dust component results in a luminosity production of $1.1 \times 10^9 {}^{+3.9 \times 10^8}_{-2.0 \times 10^8}$ L$_\odot$.

In order to test the accuracy of this method we also computed the "warm" dust luminosity by integrating the residual fluxes but, this time, assuming a linear interpolation for the residual fluxes at the specific wavelengths (Fig. 5). With this method we compute a "warm" dust luminosity of $1.0 \times 10^9 {}^{+3.0 \times 10^8}_{-3.1 \times 10^8}$ L$_\odot$. A more detailed comparison, on a pixel by pixel basis, between the two methods for determining the "warm" dust luminosity, as described above, is given in Fig. 6 with the histograms of the luminosity density (in units of L$_\odot$ pc$^{-2}$) presented for the two cases discussed above. For comparison, the histogram of the "cool" luminosity density is also plotted. From these histograms, one can see that the distribution of the luminosity densities using the two methods is very similar with the "constant" interpolation approach giving a slightly broader distribution compared to the "linear" one.

A further check that we did in order to investigate the accuracy of our method was to compute the luminosity values for the two components by using the total fluxes for the galaxy (integrated within an ellipse with a semi-major axis length of 8 kpc). With this approach both the "cool" and the "warm" components could be calculated (see Kramer et al. 2010) resulting in a "cool" dust luminosity of $9.3 \times 10^8 {}^{+3.7 \times 10^8}_{-2.2 \times 10^8}$ L$_\odot$ and a "warm" dust luminosity of $7.4 \times 10^8 {}^{+2.6 \times 10^8}_{-5.4 \times 10^8}$ L$_\odot$ (see upper left panel in Fig. 4).

As a final test, we computed the total luminosity of M33 following the recipe presented in Boquien et al. (2011). With this approach the total IR luminosity was computed by fitting the Draine & Li model to the data (IRAC, MIPS, PACS, SPIRE). As a product of this method, scaling relations were produced between surface brightness measurements at specific wavelengths and the total IR luminosity. For our purpose we choose to use the 250 $\mu$m surface brightness map which is the one with the best signal-to-noise. After calculating the total IR luminosity and subtracting the already estimated "cool" dust luminosity we find a "warm" luminosity of $8.4 \times 10^8$ L$_\odot$.

Given the large differences between the methods discussed above, the values for the "warm" dust luminosity are very similar, within the computed uncertainties, giving us a high confidence that this part of the luminosity, although estimated with very simple methods, is an accurate first approximation. For the analysis to follow we make use of the luminosity calculations derived with the "constant" interpolation method since with this method the total "warm" luminosity is closer to the values derived by both the Boquien et al. (2011) method and the integrated fluxes method. With this method the total luminosity of the
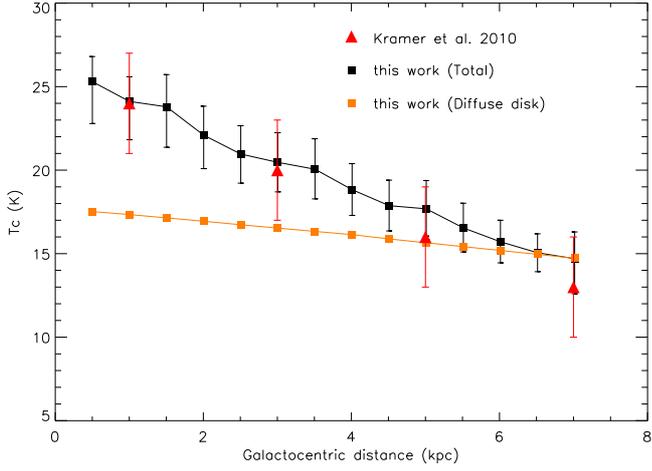
**Fig. 9.** Azimuthally averaged radial profile of the "cool" temperature for the whole galaxy (black sqares) and for the disk only (orange squares; see Sect. 6.2). For comparison, the "cool" dust temperatures for the dust that were calculated in Kramer et al. (2010) for a two-component modified blackbodies model with $\beta = 1.5$ and for the radial anulii: $0 < R < 2$ kpc, $2 < R < 4$ kpc and $4 < R < 6$ kpc are also presented (red triangles).
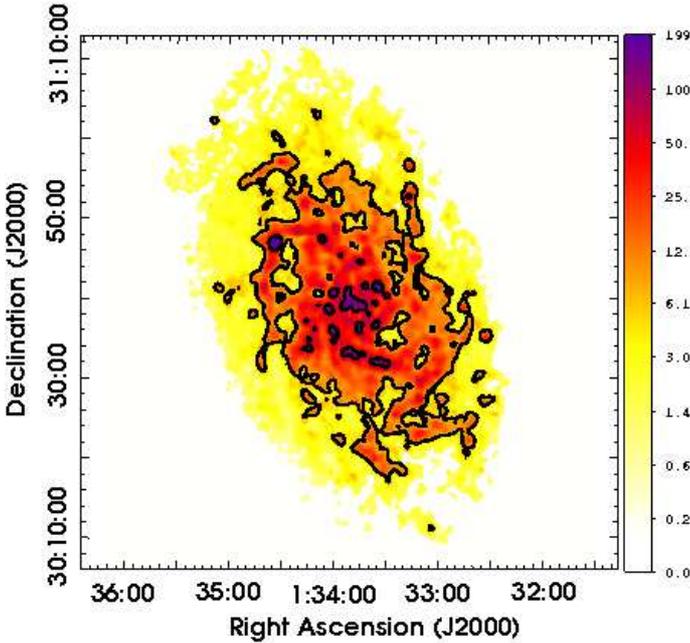


**Fig. 10.** The luminosity map of M 33 produced by the "cool" dust grains. Luminosities less than 7 $L_\odot pc^{-2}$ (yellow areas) are found in the outer diffuse parts of the galaxy while higher luminosities trace the spiral arms (orange/red areas). The highest luminosity densities ($> 90$ $L_\odot pc^{-2}$; innermost contours; blue areas) are produced in the bright HII regions and the center of the galaxy.

galaxy (integrated in the 5 - 1000 $\mu$m wavelength range) is $(1.9 \times 10^9 \, ^{+4.0\times10^8}_{-4.4\times10^8} \, L_\odot)$.



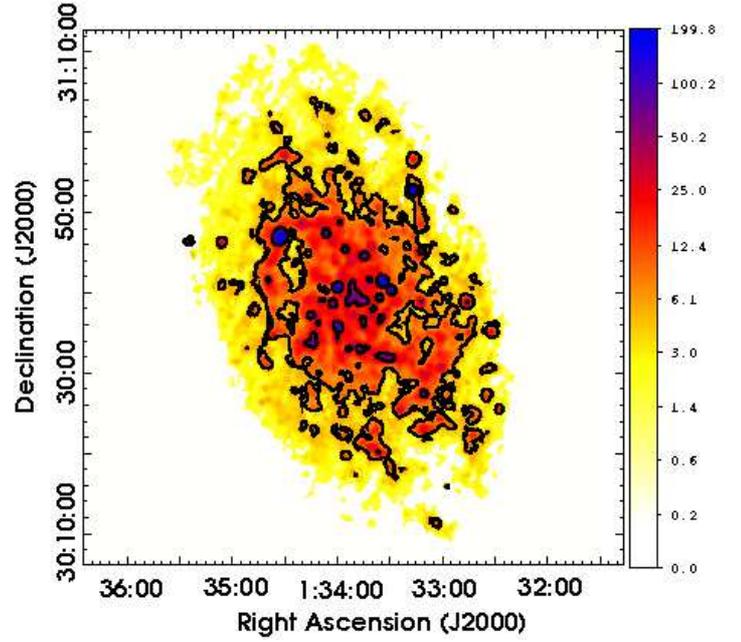**Fig. 11.** The luminosity map of M 33 produced by the "warm" dust grains. Luminosities less than 6 $L_\odot pc^{-2}$ (yellow areas) are found in the outer diffuse parts of the galaxy while higher luminosities trace the spiral arms (orange/red regions). The highest luminosity densities ($> 40$ $L_\odot pc^{-2}$; innermost contours; blue areas) are produced in the bright HII regions and the center of the galaxy. The "constant" interpolation method was used to estimate the "warm" dust luminosities.

## 5. Results

Figure 7 shows the "cool" temperature pixel map created by modeling the SED. This dust component is heated at temperatures between 11 and 28 K with $\sim$ 15 K being the most common temperature throughout the galaxy (see Fig. 8). In general, the "cool" temperature is symmetrically distributed throughout M33 with typical temperatures of $\sim$ 25 K close to the center of the galaxy, dropping to $\sim$ 15 K close to the outskirts. The spiral structure is not clearly seen in the "cool" temperature distribution (Fig. 7). The effect of the dimming of the spiral arms with respect to the large radial gradient of the galaxy is also present when looking at the 250/350 and 500/350 color maps (with the SPIRE colors being valuable indicators of the "cool" dust temperature distribution; see Fig. 4 in Boquien et al. 2011 and Fig. 1 in Braine et al. 2010). This is also evident when looking at the azimuthally averaged profile of the temperature (black line in Fig. 9) showing a monotonic decrease from the center to the outskirts with no obvious variations from, e.g., the spiral structure. For comparison, the "cool" dust temperature values calculated by Kramer et al. (2010) but for a range of elliptical annuli are also plotted (red triangles). In general, the values are within the errors for the temperature. The slightly higher temperatures that we calculate are due to the small differences in the calibration of the Herschel data set that was used in Kramer et al. (2010).

Temperatures with T < 18 K (yellow areas in Fig. 7) are found in the outer parts of the galaxy while larger temperatures trace the inner part of the galaxy. The highest temperatures (T > 23 K; innermost contour; blue areas in
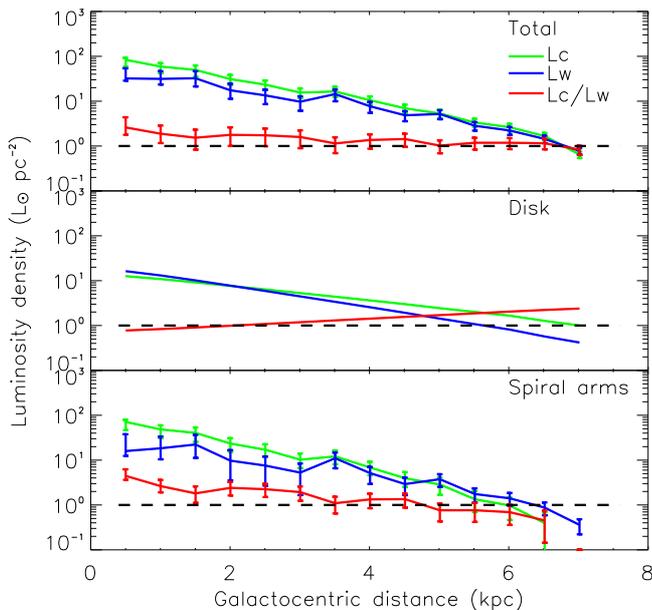
**Fig. 12.** The azimuthally averaged profiles of the "cool" and the "warm" dust luminosities (green and blue lines) in units of $L_\odot pc^{-2}$. The cool-to-warm luminosity ratio is also plotted (red line). The luminosities are calculated for the whole galaxy (upper panel) and for the disk of the galaxy only (middle panel; see Sect. 6.2). The residuals between the two profiles give the radial distribution of the luminosity produced by the spiral arm network (bottom panel).

Fig. 7) are found in individual HII regions and the center of the galaxy. This picture is also evident when examining individual SEDs like the ones presented in Fig. 4 with temperatures in the ranges discussed above for the HII regions (like, e.g., NGC 604), the center of the galaxy, and the diffuse outskirts regions of the galaxy. In these cases the best fit temperatures and the 90% confidence limits obtained with this model are $31.5^{+1.6}_{-5.1}$ K for the NGC 604 region, $25.4^{+1.0}_{-1.8}$ K for the central region of the galaxy, and $15.7^{+4.7}_{-3.0}$ K in the outer, diffuse, parts of the galaxy. These are typical values of the temperature for the various regions throughout the galaxy giving also an estimate of the accuracy of the fitted parameters. Given the simplicity of our SED model, and especially in the MIR wavelengths (below $\sim 70~\mu m$), where significant contribution to the emission from stochastically heated dust grains is expected, we investigated the effects of omitting the 70 $\mu m$ fluxes from the analysis. In this way the "cool" dust component is constrained by observations at wavelengths greater than 100 $\mu m$. We find that the "cool" dust temperature changes only slightly (variations of less than 2%) well within the estimated uncertainties. This gives us enough confidence on the "cool" dust component calculation.

For the "warm" dust component we do not present a temperature map since, as already stressed before, the temperature of this component, as derived from a two modified blackbodies fit, can be highly uncertain in many regions throughout the galaxy (especially the bright ones; see the upper right and lower left panels in Fig. 4). It is worth mentioning though that, when considering the galaxy as a whole, the "warm" dust temperature can be calculated

and is $55.0^{+2.5}_{-3.7}$ K (in accordance to previous studies, e.g., Kramer et al. 2010) while for a typical, low brightness region (like the one in the lower right panel of Fig. 4) the temperature is $51.0^{+2.9}_{-2.3}$ K.

The "cool" dust luminosity (Fig. 6 and 10) varies between $\sim 0.3~L_\odot pc^{-2}$ and $\sim 800~L_\odot pc^{-2}$ with a value of $\sim 1.7~L_\odot pc^{-2}$ accounting for most parts across the galaxy. Luminosities less than 7 $L_\odot pc^{-2}$ (yellow areas in Fig. 10) are produced in the diffuse parts on the outermost regions of the galaxy while higher luminosities (orange/red areas in Fig. 10) are emitted from the spiral arms. The highest luminosity densities (L > 90 $L_\odot pc^{-2}$; innermost contours (blue areas) in Fig. 10) are produced by the HII regions and the center of the galaxy. This is also indicated when looking at individual SEDs inside the galaxy (Fig. 4) resulting in a "cool" dust luminosity of $819^{+84}_{-415}~L_\odot pc^{-2}$ for NGC 604, $114^{+12}_{-24}~L_\odot pc^{-2}$ for the center and $2.2^{+2.4}_{-0.95}~L_\odot pc^{-2}$ for the outer parts of the galaxy.

The "warm" dust luminosity (Fig. 6 and 11) varies between $\sim 0.3~L_\odot pc^{-2}$ and $\sim 400~L_\odot pc^{-2}$ with a value of $\sim 1.6~L_\odot pc^{-2}$ accounting for most parts across the galaxy. Luminosities less than 7 $L_\odot pc^{-2}$ (yellow areas in Fig. 11) are produced in the diffuse parts of the galaxy while higher luminosities are emitted from the spiral arms (orange/red areas in Fig. 11). The highest luminosity densities (L > 40 $L_\odot pc^{-2}$; innermost contours (blue areas) in Fig. 11) are produced by the HII regions and the center of the galaxy. This map has been computed by assuming the "constant" interpolation method for estimating the "warm" dust luminosity (see Sect. 4.1). As in the case of the "cool" dust luminosity (discussed above) individual SEDs indicate luminosities, produced by the "warm" dust material, of $404^{+380}_{-67}~L_\odot pc^{-2}$ for NGC 604, $42^{+18}_{-27}~L_\odot pc^{-2}$ for the center and $2.8^{+0.6}_{-1.97}~L_\odot pc^{-2}$ for the outer parts of the galaxy.

## 6. Discussion

### 6.1. The "warm" and the "cool" dust distribution

Comparison of the "cool" and the "warm" luminosity maps in Figs 10 and 11 indicates that the morphology is very similar for the two dust components with the spiral structure clearly seen in both cases and with local enhancements in the areas where the HII regions reside. This similarity becomes more striking when looking at the azimuthally averaged radial profiles (upper panel in Fig. 12) of the luminosity densities of the two components (green and blue lines for the "cool" and the "warm" components) and their ratio ($L_c/L_w$; red line). From this profiles it is evident that, given the uncertainties of the computed luminosities, the "cool" dust luminosity is the dominant source of luminosity in the central parts of the galaxy (with the "cool" luminosity being $\sim 3$ times more than the "warm" luminosity) while the ratio gets rather flat and close to unity beyond a $\sim 3$ kpc radius. This narrow range of the ratio (close to unity) of the two luminosities suggests that both dust components (the "cool" dust heated at $\sim 15$ K and the "warm" dust heated at $\sim 55$ K) are able to produce about the same amounts of luminosities throughout the galaxy.

Approximating the azimuthally averaged radial profiles of the two luminosities with exponential functions, we find that they decay with scalelengths of 2.59±0.04 kpc for the "cool" dust and 1.77±0.02 kpc for the "warm"

**Table 1.** "Warm" and "cool" dust luminosities for the total galaxy, for the disk of the galaxy and for the spiral arms of the galaxy.

| Total galaxy |
|---|
| $L_{total}$=1.9 $\times10^9 L_\odot$ |
| $L_w$=7.8 $\times10^8 L_\odot$ (41% $L_{total}$) |
| $L_c$=1.1 $\times10^9 L_\odot$ (59% $L_{total}$) |
| **Disk** |
| $L_{disk}$=5.7 $\times10^8 L_\odot$ (30% $L_{total}$) |
| $L_{disk}^w$=2.5 $\times10^8 L_\odot$ (32% $L_w$, 44% $L_{disk}$) |
| $L_{disk}^c$=3.2 $\times10^8 L_\odot$ (29% $L_c$, 56% $L_{disk}$) |
| **Spiral Arms** |
| $L_{spiral}$=1.3 $\times10^9 L_\odot$ (70% $L_{total}$) |
| $L_{spiral}^w$=5.3 $\times10^8 L_\odot$ (68% $L_w$, 40% $L_{spiral}$) |
| $L_{spiral}^c$=7.8 $\times10^8 L_\odot$ (71% $L_c$, 60% $L_{spiral}$) |

dust. Comparing with the scalelengths that we have derived for individual wavelengths (Sect. 3 and this section) we see that the "warm" dust luminosity is very similar to the values derived for the MIR/FIR wavelengths while the "cool" dust luminosity has a scalelength similar to the 250-500 $\mu$m submm wavelengths. This directly implies that the "cool" dust grains (mostly contributing to the "cool" part of the luminosity of the galaxy) emit in the submm wavelengths while the "warm" dust grains emit in the MIR/FIR wavelengths shaping up the "warm" part of the luminosity of the galaxy.

## 6.2. Decomposing M33 into a disk and a spiral arm network

The dust distribution inside a galaxy can be quite inhomogeneous. When considering the morphology in a large scale the dust distribution can be approximated by a superposition of a diffuse disk and a spiral arm network (see e.g. Xilouris et al., 1999, Misiriotis et al. 2000; Meijerink et al. 2005). As a first order approximation the diffuse disk can be quite accurately described by a three-dimensional disk decreasing exponentially both in the radial and in the vertical directions:

$$\eta(R,z) = \eta_0 \exp(-\frac{R}{h_d} - \frac{|z|}{z_d}) \qquad (2)$$

where $\eta_0$ is the dust volume density at the nucleus of the galaxy and $h_d$ and $z_d$ are the scalelength and scaleheight of the dust respectively (see Xilouris et al. 1999). We make use of this simple model to delineate between the two main dust components (i.e. the the dust that is diffusely distributed in a disk throughout the galaxy revealing itself in the inter-arm regions of the galaxy and the dust that is forming the spiral arms).

Determining the scaleheight of the dust is not trivial since, unlike edge-on galaxies where the vertical extent of the dust can be measured, in less inclined galaxies, like M33, this parameter cannot be easily determined. We note however that for our study, where we aim at calculating the relative fraction of the fluxes and luminosities emitted by the diffuse and the spiral arm network, the choice of the scaleheight is not a crucial issue. This is because the total luminosity of the disk is independent of $z_d$ (a larger value of $z_d$ (thicker disk) would require a smaller value of $\eta_0$ (fainter disk) in order to fit the data which, at the end, results in the same luminosity; see Xilouris et al. 1997). For the purposes
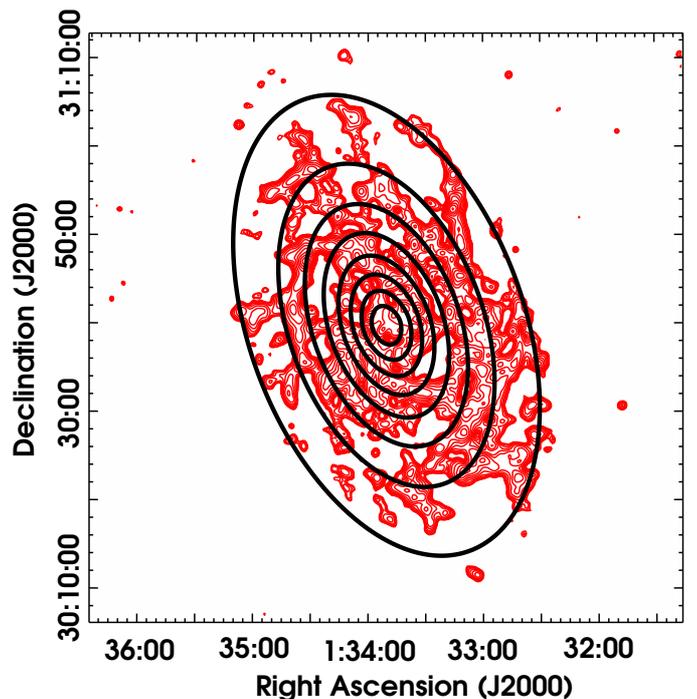


**Fig. 13.** The 250 $\mu$m image of M33 decomposed into a diffuse axisymmetric disk (black contours) and its spiral structure network (red contours; see the text for more details).
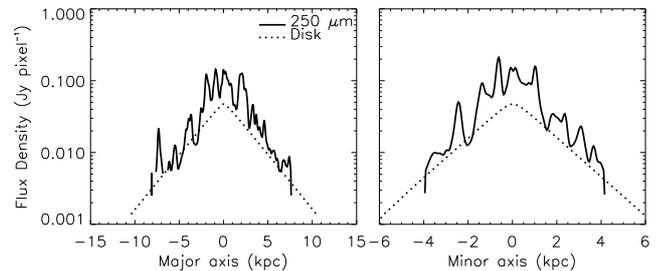


**Fig. 14.** The 250 $\mu$m profile of M33 along the major axis (left) and the minor axis (right). In both cases the solid line corresponds to the observed emission while the dotted line is the exponential disk fitted to the data.

of this study we use a scaleheight of $z_d = 0.2$ kpc. This is a typical scaleheight that describes the diffuse dust in a galaxy derived from modeling and observations of edge-on galaxies (Xilouris et al. 1999; Bianchi & Xilouris 2011). In particular, for M33, this is close to the value derived by Combes et al. (2012) using a power spectrum analysis.

For the scalelength we use the values determined by fitting the azimuthally averaged profiles (see Sect. 3, Fig. 2). Since we also want to investigate the origin of the emission in the MIR wavelengths we perform the analysis for the scalelength determination (described in Sect. 3) in the MIPS-24 and 70 $\mu$m. We find scalelength values of $1.87 \pm 0.09$ and $1.90 \pm 0.05$ kpc respectively for the 24 and 70 $\mu$m emission.

With the scalelengths and scaleheights of the disk fixed the three dimensional model is then inclined by 56 degrees

9

(the inclination angle of M33) and the integrated, along the line of sight, intensities of the model are fitted to the galaxy maps in a pixel-by-pixel basis. We use only the fluxes in the outermost regions of the galaxy and in the inter-arm regions (the areas with minimum values in between the obvious spiral structure) in order to constrain the emissivity at the galactic center ($\eta_0$). We do this since we only want to fit the diffuse part of the galaxy and avoid the spiral arms and the more complex structures that are superimposed on the diffuse disk. The fit was done by minimizing the $\chi^2$ values in a similar procedure with what is described in Sect. 4.

An example of this analysis is presented in Fig. 13 showing the 250 $\mu$m map decomposition. In this figure, the black contours show the axisymmetric exponential disk that is fitted to the data (Eq. 2) while the red contours show the spiral arm network determined after subtracting the map of the diffuse disk from the observed image. In more detail this decomposition can be seen in Fig. 14 with the radial profiles of the fitted disk to the 250 $\mu$m data (dotted lines) along with the observed major- and minor-axis profiles (left and right panel respectively). From these profiles it is clear that the spiral arms are superimposed on the disk allowing for a clear separation of the two components.

Using the available Spitzer and Herschel maps of M33 we find that the flux that is emitted from the disk accounts for 21, 29, 38, 42, 48, 52, and, 57% of the total flux for the 24, 70, 100, 160, 250, 350, and 500 $\mu$m respectively. We see that in the MIR wavelengths it is the spiral structure which is the dominant source of emission while, at around $\sim$ 250 $\mu$m the emission comes equally from both the disk and the spiral arms. In contrast, the dominant source of the submm emission is the disk of the galaxy.

Having calculated the emission that is produced by the diffuse dust disk in all available bands, we can then calculate the temperature and the luminosity of this component separately. We do so by applying the SED modeling that we did for the whole galaxy (Sect. 4) but now for this component only.

For the "cool" temperature in the disk we find a very narrow distribution (compared to the galaxy as a whole) with values ranging between 15 and 18 K. This is shown in Fig. 8 with the dark blue distribution being that of the diffuse disk. Given a typical 3 K uncertainty for the temperature distribution the disk temperatures occupy the lower end of the temperature distribution for the whole galaxy (light blue) leaving the higher temperatures ($> 18$ K) accounting for the rest of the galaxy (spiral arms and HII regions). The narrow range in temperatures is also seen in Fig. 9 with temperatures of $\sim$ 18 K in the center of the galaxy dropping to $\sim$ 15 K at the edges. A similar narrow range of temperatures for the diffuse dust in the disk of the Milky Way has been derived based on COBE observations. Temperatures for the diffuse cirrus component ranging from 17 K to 21 K are found using FIR color maps (e.g. Reach et al. 1995; Schlegel et al. 1998) while a 15 K to 19 K range has been computed for the disk of the Milky Way via radiative transfer modeling (Misiriotis et al. 2006). Similar findings have been recently derived using Herschel observations of the galactic plane indicating that the warmest dust is located in the spiral arms (Bernard et al. 2010). The narrow range of the temperatures that we find in the disk of M33 is consistent with this picture, with the disk primarily hosting the cirrus dust component which is heated by the diffuse interstellar radiation field. On the other hand, the dust in the

spiral arms is embedded in more dense environments, and is, mainly, heated by the local UV radiation of the young stars, allowing for a wider range of temperatures. We note however that a more detailed analysis, taking into account both the exact radiation field that is heating the dust as well as the dust composition and density in various places throughout the galaxy is clearly needed for a proper characterizing the properties of the interstellar dust in different environments.

Concerning the luminosity, we find that $5.7 \times 10^8$ L$_\odot$ (30% of the total luminosity) is produced by the dust in the disk. This indicates that the dominant source of the luminosity of the galaxy in the infrared/submm wavelengths is the spiral arm network. Furthermore, looking at the "warm" and the "cool" components separately we compute that the dust that resides in the disk and is "warm" emits $2.5 \times 10^8$ L$_\odot$ which is 32% of the total "warm" dust luminosity while the "cool" dust material produces $3.2 \times 10^8$ L$_\odot$ which is 29% of the total "cool" dust luminosity. All the above results, as well as the values derived for the spiral arms, are summarized in Table 1

The above results indicate that when considering the luminosities of the "warm" and the "cool" dust their origin is mainly the spiral arm network which produces 71% of the luminosity of the "cool" and 68% of the luminosity of the "warm" dust of the galaxy. Furthermore, 41% of the total luminosity of the galaxy is emitted by "warm" grains while the rest 59% is emitted by "cool" dust grains. These percentages are about the same when separating the disk from the spiral arms. We see, for example, that inside the disk 44% of the luminosity is emitted by the "warm" dust compared to 56% which is emitted by the "cool" dust and, similarly for the spiral arms, 40% comes from the "warm" and 60% from the "cool" dust.

It is interesting to further investigate the relative distribution of the "warm" and "cool" luminosities that reside inside the disk and the spiral arms as a function of galactocentric radius. The decomposition of the azimuthally averaged radial profiles is shown in Fig. 12 with the disk profiles presented in the middle panel and the spiral arm profiles in the bottom panel. The disk profiles (middle panel) are derived by fitting the two modified blackbodies model to the smooth disk maps in each available wavelength. These maps are derived by fitting the three-dimensional model (Eq. 2) to the observations as described earlier. From these profiles it is evident that the "cool" dust in the disk of the galaxy becomes the dominant component in the outer parts of the galaxy (beyond $\sim$ 3 kpc) while the "cool" dust is the main source of luminosity production within the inner $\sim$ 3 kpc inside the spiral arm network.

## 7. Conclusions

Through modeling of the SED of the local group galaxy M33 and exploiting the unique wavelength coverage and sensitivity of the Herschel 100, 160, 250, 350 and 500 $\mu$m observations, as well as additional Spitzer-IRAC 5.8 and 8 $\mu$m and Spitzer-MIPS 24 and 70 $\mu$m data, we derive the following conclusions on the dust emission of the galaxy:

− The submm emission from M33 is distributed in a flatter way (scalelength of 3.04 kpc at 500 $\mu$m) compared to the far-infrared emission (scalelength of 1.84 kpc at 100 $\mu$m).

- On average, the emission by the dust can be adequately modeled by a superposition of two modified blackbodies with $\beta = 1.5$.
- The temperature of the "cool" grains ranges between 11 and 28 K with a most common value of $\sim 15$ K across the galaxy.
- The total luminosity of the galaxy (integrated from 5 to 1000 $\mu$m) is $1.9 \times 10^9$ $^{+4.0\times10^8}_{-4.4\times10^8}$ $L_\odot$ with the luminosity of the "cool" dust component accounting for 59% of the total luminosity.
- The scalelength of the "cool" ("warm") luminosity distribution is very similar to that of the submm (MIR/FIR) emission. This similarity directly reflects the important wavelengths that contribute the most in each of the two luminosity components.
- Decomposing the galaxy into two components (namely, a diffuse disk and a spiral-arm network) we find that the emission in the disk accounts for $\sim 21\%$ in the MIR wavelengths (24 $\mu$m) while it gradually rises to $\sim 57\%$ in the submm wavelengths (500 $\mu$m).
- The "cool" dust material in the disk of the galaxy, presumably accounting for the cirrus dust component of the galaxy, is heated at temperatures between $\sim 15$ K at the edges of the galaxy to $\sim 18$ K at the center.
- The bulk of the luminosity is emitted by the spiral arm network ($\sim 70\%$) and this percentage stays roughly the same when considering the "warm" and the "cool" dust luminosities separately.
- About $\sim 40\%$ of the total luminosity throughout the galaxy (and separately inside the disk and the spiral arms) is emitted by the "warm" dust grains with the rest $\sim 60\%$ emitted by the "cool" dust.
- The ratio of the "cool" to "warm" dust luminosity is close to unity throughout most of the the galaxy but slightly enhanced within the central $\sim 3$ kpc of the galaxy.
- The "cool" dust inside the disk becomes dominant in the outer parts of the galaxy (beyond $\sim 3$ kpc).
- The "cool" dust inside the spiral arms become dominant in the inner parts of the galaxy (within $\sim 3$ kpc).

# References

Alton, P.B, Trewhella, M., Davies, J.I., et al. 1998, 335, 807
Aniano, G.J., Draine, B.T., Gordon, K.D., & Sandstrom, K. 2011, PASP, 123, 1218
Bendo, G.J., Wilson, C.D., Pohlen, M., et al. 2010, 518, 65
Bendo, G.J., Boselli, A., Dariush, A., et al. 2012, MNRAS, 419, 1833
Benford, D.J., & Staguhn, J.G. 2008, ASPC, 381, 132
Bernard, J.-Ph., Paradis, D., Marshall, D.J., et al. 2010, A&A, 518, L88
Bevington, P., & Robinson, D. 1992, Data reduction and error analysis for the physical sciences (McGraw-Hill, Inc.)
Bianchi, S., & Xilouris, E.M. 2011, A&A, 531, 11
Binney J., & Tremaine S. 1987, Galactic Dynamics. Princeton Univ. Press, Princeton
Block, D. L, Combes, F., Puerari, I., et al. 2007, A&A, 471, 467
Block, D. L., Elmegreen, B. G., Wainscoat, R. J. 1996, *Nat.*, 381, 674
Boquien, M., Calzetti, D., Combes, F., et al. 2011, AJ, 142, 111
Boquien, M., Calzetti, D., Kramer, C., et al. 2010, A&A, 518, 70
Braine, J., Gratier, P., Kramer, C., et al. 2010, A&A, 518, 69
Combes, F., Boquien, M., Kramer, C., et al. 2012, A&A, 539, 67

Davies, J.I., Alton, P., Trewhella, M., Evans, R., & Bianchi, S. 1999, MNRAS, 304, 495
Devereux, N. A., & Young, J. S. 1990, ApJ, 359, 42
Dunne, L., & Eales, S. A. 2001, MNRAS, 327, 697
Freedman, W. L., Wilson, C. D., & Madore, B. F. 1991, ApJ, 372, 455
Gerola, H., & Seiden, P. E. 1978, ApJ, 223, 129
Gordon, K.D., Bailin, J., Engelbracht, C.W., et al. 2006, ApJ, 638, 87
Gratier, P., Braine, J., Rodriguez-Fernandez, N.J., et al. 2011, arXiv1111.4320
Gratier, P., Braine, J., Rodriguez-Fernandez, N.J., et al. 2010, A&A, 522, 3
Griffin, M., Abergel, A., Abreu, A., et al. 2010, A&A, 518, 3
Haas M., Lemke, D., Stickel, M., et al. 1998, A&A, 338, 33
Hippelein, H., Haas, M., Tuffs, R. J., et al. 2003, A&A, 407, 137
Hoopes, C.G., & Walterbos, R.A.M. 2000, ApJ, 541, 597
Kramer, C., Buchbender, C., Xilouris, E.M., et al. 2010, A&A, 518, 67
Kramer, C., Richer, J., Mookerjea, B., Alves, J., & Lada, C. 2003, A&A, 399, 1073
Krüegel, E. 2003, The physics of interstellar dust, ed. Krüegel, E.
Krüegel, E., & Siebenmorgen, R. 1994, A&A, 288, 929
Meijerink, R., Tilanus, R.P.J., Dullemond, C.P., Israel, F.P., van der Werf, P.P. 2005, A&A, 430, 427
Misiriotis, A., Kylafis, N.D., Papamastorakis, J., & Xilouris, E.M. 2000, A&A, 353, 117
Ott, D. 2010, ASP Conf. Ser., 434, 139
Paturel, G., Petit, C., Prugniel. P., et al. 2003, A&A, 412, 45
Pilbratt, G.L., Riedinger, J.R., Passvogel, T., et al. 2010, A&A, 518, 1
Poglitsch, A., Waelkens, C., Geis, N., et al. 2010, A&A, 518, 2
Press W.H., Flannery B.P., Tenkolsky S.A., & Vetterling W.T. 1986, Numerical Recipes, Cambridge Univ. Press, Cambridge
Reach, W. T., Dwek, E., Fixsen, D. J., et al. 1995, ApJ, 451, 188
Regan, M. W., & Vogel, S. N. 1994, ApJ, 434, 536
Roussel, H., 2012, A&A, submitted
Schlegel, D. J., Finkbeiner, D. P., & Davis, M. 1998, ApJ, 500, 525
Tabatabaei, F. S., Beck, R., Krause, M., et al. 2007a, A&A, 466, 509
Tabatabaei, F. S., Beck, R., Krügel, E., et al. 2007b, A&A, 475, 133
Tabatabaei, F. S., Braine, J., Kramer, C., et al. 2011, arXiv1111.6740
Verley, S., Relaño, M., Kramer, C., et al. 2010, A&A, 518, 68
Verley, S., Corbelli, E., Giovanardi, C., & Hunt, L. K. 2009, A&A, 493, 453
Verley, S., Hunt, L. K., Corbelli, E., & Giovanardi, C. 2007, A&A, 476, 1161
Xilouris E.M., Byun, Y.I., Kylafis, N.D., Paleologou, E.V., & Papamastorakis, J. 1999, A&A, 344, 868
Yang, M., & Phillips, T. 2007, ApJ, 662, 284
Young, J. S., Allen, L., Kenney, J. D. P., Lesser, A., & Rownd, B. 1996, AJ, 112, 1903

[1] Institute for Astronomy, Astrophysics, Space Applications & Remote Sensing, National Observatory of Athens, P. Penteli, 15236 Athens, Greece

[2] Max-Planck-Institut für Astronomie, Königstuhl 17, D-69117 Heidelberg, Germany

[3] Laboratoire d'Astrophysique de Marseille - LAM, Université d'Aix-Marseille & CNRS, UMR7326, 38 rue F. Joliot-Curie, 13388, Marseille Cedex 13, France

[4] Instituto Radioastronomia Milimetrica (IRAM), Av. Divina Pastora 7, Nucleo Central, E-18012 Granada, Spain

[5] Argelander Institut fr Astronomie. Auf dem Hügel 71, D-53121 Bonn, Germany

[6] Laboratoire d'Astrophysique de Bordeaux, Université Bordeaux 1, Observatoire de Bordeaux, OASU, UMR 5804, CNRS/INSU, B.P. 89, Floirac F-33270

[7] Departamento de Física Teórica y del Cosmos, Universidad de Granada, Campus Fuentenueva, Granada, Spain

[8] Instituto de Astronomía, UNAM, Campus Ensenada México

[9] Max-Planck-Institut für Radioastronomie (MPIfR), Auf dem Hügel 69, D-53121 Bonn, Germany

[10] Department of Astronomy, University of Massachusetts, Amherst, MA 01003, USA

[11] Observatoire de Paris, LERMA, CNRS, 61 Av. de l'Observatoire, 75014 Paris, France

[12] Institut de Radioastronomie Millimétrique, 300 rue de la Piscine, 38406 Saint Martin d'Hères, France

[13] Astronomy Department, King Abdulaziz University, P.O. Box 80203, Jeddah, Saudi Arabia

[14] Leiden Observatory, Leiden University, PO Box 9513, 2300 RA Leiden, The Netherlands

[15] Australia Telescope National Facility, CSIRO, PO Box 76, Epping, NSW 1710, Australia

[16] Infrared Processing and Analysis Center, MS 100-22 California Institute of Technology, Pasadena, CA 91125, USA

[17] Department of Astronomy & Astrophysics, Tata Institute of Fundamental Research, Homi Bhabha Road, Mumbai 400005, India

[18] University of British Columbia Okanagan, 3333 University Way, Kelowna, BC V1V 1V7, Canada

[19] Department of Astronomy, Cornell University, Ithaca, NY 14853, USA

[20] Joint Astronomy Centre, 660 North A'ohoku Place, University Park, Hilo, HI 96720, USA

[21] Netherlands Organization for Scientific Research, Laan van Nieuw Oost-Indie 300, NL2509 AC The Hague, The Netherlands

[22] SRON Netherlands Institute for Space Research, Landleven 12, 9747 AD Groningen, The Netherlands

[23] SUPA, Institute for Astronomy, University of Edinburgh, Royal Observatory, Blackford Hill, Edinburgh EH9 3HJ, UK